

Article

Sn-TiO₂/PTA Nanocomposite Films for High-Contrast Rewritable Media with Visible-Light-Driven Black Coloration

Yao Dou, Dongliang Wei, Yongli Qin, Zhen Zhang, Yun Zhang *, and Wenshou Wang *

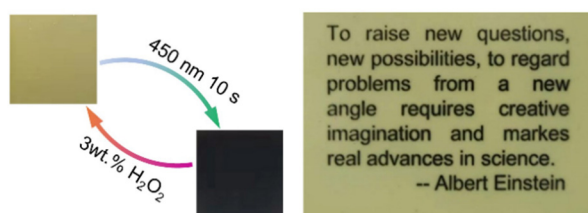
School of Chemistry and Chemical Engineering, University of Jinan, Jinan 250022, China

* Correspondence: chm_zhangy2022@ujn.edu.cn (Y.Z.); chm_wangws@ujn.edu.cn (W.W.)

Received: 19 March 2025; Revised: 21 April 2025; Accepted: 23 April 2025; Published: 15 May 2025

Abstract: Photochromic materials are pivotal for rewritable smart media, yet conventional systems suffer from sluggish kinetics, UV dependency, and low optical contrast. Herein, we present a visible-light-responsive Sn-TiO₂/phosphotungstic acid (PTA) nanocomposite film mediated by polyvinylpyrrolidone (PVP) that addresses these challenges through

interfacial engineering and bandgap modulation. Sn-doped TiO₂ nanoparticles, synthesized hydrothermally, are covalently linked to phosphotungstic acid (PTA) clusters via PVP-assisted dispersion, enabling efficient charge separation under 450 nm illumination. The Sn-TiO₂/PTA/PVP nanocomposite film achieves ultrafast coloration within 10 s, attributed to the reduction of W⁶⁺ to W⁵⁺ in PTA. The colored state exhibits remarkable air stability (48 h) and rapid recovery (<30 min) via H₂O₂ vapor, sustaining >80 reversible cycles without degradation. With a narrowed bandgap (2.23 eV) and broadband intervalence charge transfer (IVCT) absorption (600–800 nm), the film demonstrates high-contrast black-state coloration and 2-day legibility as a rewritable medium. This work overcomes the limitations of organic dyes and UV-dependent systems, offering an inorganic, eco-friendly platform for smart displays, anti-counterfeiting labels, and energy-efficient photochromic technologies.



Keywords: photochromic nanocomposites; visible-light response; Sn-doped titanium dioxide; phosphotungstic acid; rewritable smart media

1. Introduction

Photochromic materials, capable of reversible color changes under external stimuli, have emerged as critical components in smart windows [1–5], rewritable media [6–12], and anti-counterfeiting systems [13–18]. Among inorganic photochromic candidates, transition metal oxides (e.g., WO₃, MoO₃, TiO₂) and polyoxometalates (POMs) dominate due to their thermal stability, environmental robustness, and tunable redox properties [19–25]. However, conventional systems face intrinsic limitations: (i) narrow visible-light absorption (typically <450 nm) due to wide bandgaps [26–28], (ii) sluggish coloration/bleaching kinetics caused by inefficient charge separation [29], and (iii) low optical contrast due to their characteristic blue/gray coloration, which reduces readability under ambient lighting [30]. For instance, Zhang et al. [31] reported UV-driven TiO₂/PMoA rewritable paper with a 70-cycle lifespan, yet its reliance on UV light and blue-phase coloration pose safety concerns and visual limitations, such as poor legibility under white-light illumination. These unresolved challenges underscore the need for material systems that simultaneously achieve visible-light activation, rapid switching kinetics, and high-contrast optical states.

Recent advancements focus on enhancing light absorption and charge transfer efficiency through nanostructuring [32,33], heterojunction engineering [34–36], and doping strategies [5,37,38]. Sn-doped TiO₂ (Sn-TiO₂), for example, demonstrates extended visible-light response (up to 450 nm) by introducing intermediate energy levels via Sn⁴⁺ substitution, which introduces intermediate energy levels to narrow the bandgap [39]. Concurrently, phosphotungstic acid (PTA, H₃PW₁₂O₄₀), a Keggin-type POM, exhibits reversible redox activity and structural integrity during coloration [29,40,41]. Xiong et al. [42] developed PTA-polyurethane films with UV-triggered photochromism, yet their reliance on UV light and slow recovery (>5 h) limit scalability. Hybrid



Copyright: © 2025 by the authors. This is an open access article under the terms and conditions of the Creative Commons Attribution (CC BY) license (<https://creativecommons.org/licenses/by/4.0/>).

Publisher's Note: Scilight stays neutral with regard to jurisdictional claims in published maps and institutional affiliations.

systems combining Sn-TiO₂ with organic dyes (e.g., neutral red) partially address visible-light activation [39], but organic components degrade rapidly under prolonged irradiation and fail to achieve black-state coloration due to narrow absorption bands. Despite these efforts, achieving inorganic composites with integrated fast color switching, black-state optical contrast, and visible-light-driven photochromism remains a formidable challenge.

A critical yet underexplored aspect lies in achieving a high contrast black-state through tailored IVCT absorption. While reduced POMs typically exhibit broad absorption in the near-infrared region (600–800 nm) [43–45], their integration with visible-light-active semiconductors could enable intense black coloration by spanning the entire visible spectrum. However, this requires precise interfacial engineering to maximize electron transfer efficiency and minimize parasitic absorption losses. Recent studies on polyvinyl alcohol-polyethyleneimine-PTA (PVA-PEI-PTA) composites achieved grey mauve [41], but their limited IVCT bandwidth and insufficient electron density prevented true black-state formation. Thus, designing a material system that synergizes visible-light absorption, efficient charge transfer, and broadband IVCT transitions is essential for high-contrast photochromic applications.

In this work, we propose a PVP-mediated Sn-TiO₂/PTA nanocomposite film that synergizes visible-light absorption, efficient charge transfer, and black-state optical contrast. By employing PVP as both a dispersant and interfacial stabilizer, Sn-TiO₂ nanoparticles and PTA clusters are uniformly integrated, enabling enhanced charge separation while suppressing recombination. This architecture enables dual functionality: (i) Sn⁴⁺ doping narrows the TiO₂ bandgap to 2.23 eV, extending absorption to 450 nm, and (ii) PTA acts as an electron acceptor, triggering broadband IVCT transitions between W⁵⁺ and W⁶⁺ species upon reduction. The optimized nanocomposite film achieves ultrafast coloration (10 s) under 450 nm illumination, sustains >80 reversible cycles via H₂O₂ vapor treatment, and delivers intense black coloration through synergistic visible-light absorption and IVCT transitions. As a rewritable medium, the film enables high-resolution patterning with 2-day legibility, surpassing the performance of organic dye-based and UV-dependent systems. This work establishes a sustainable, inorganic platform for smart displays and energy-efficient photochromic technologies, addressing the long-standing trade-offs between speed, contrast, and stability.

2. Experimental Part

2.1. Materials and Methods

2.1.1. Materials

Titanium (IV) ethoxide (Ti(OC₂H₅)₄, 33–35%) was purchased from Macklin Biochemical Co. Ltd., (Shanghai, China) Ethylene glycol (EG, 99.0%), tin (II) chloride dihydrate (SnCl₂·2H₂O, 98.0%), polyvinylpyrrolidone (PVP, K30), and phosphotungstic acid (PTA, H₃PW₁₂O₄₀·21H₂O, 99.9%) were purchased from Sinopharm Chemical Reagent Co. Ltd. (Shanghai, China). Hydrazine hydrate (N₂H₄·H₂O, 80%) were purchased from Tianjin Damao Chemical Reagent Factory, (Tianjin, China). Glass substrates (2.5 × 2.5 cm²) were purchased from Luoyang Nuozhuo Technology Co. Ltd. (Luoyang, China). All chemicals were analytic grade and used without any further purification during the synthesis.

2.1.2. Synthesis of Sn-TiO₂ Nanoparticles

Sn-TiO₂ nanoparticles were synthesized via a hydrothermal method. In a typical procedure, SnCl₂·2H₂O (0.216 g, 0.96 mmol) was dissolved in EG (33 mL) under magnetic stirring (500 rpm, 30 min). Ti(OC₂H₅)₄ (1 mL) was added dropwise to the solution, followed by N₂H₄·H₂O (2 mL, 80%) under continuous stirring (30 min). The mixture was transferred into a 50 mL Teflon-lined autoclave (Shanghai Yanzheng Experimental Equipment Co., Ltd., Shanghai, China) and heated at 200 °C for 36 h. Light yellow precipitates were obtained by centrifugation, washed 3 times with acetone, and then dried overnight at 60 °C.

2.1.3. Fabrication of Sn-TiO₂/PTA/PVP Nanocomposite Films

A precisely measured quantity of 14.4 mg Sn-TiO₂ nanoparticles was dispersed in a mixed solvent system containing 100 mg of 20 wt.% PVP aqueous solution, 0.6 mL EG, and 103 mg of PTA solution (5.76 g/mL). The resultant suspension underwent magnetic stirring to ensure uniform colloidal distribution. The optimized coating formulation was then deposited on pre-cleaned glass substrates (2.5 cm × 2.5 cm) followed by drying at 60 °C for 6 h to obtain the typical Sn-TiO₂/PTA/PVP nanocomposite films with Sn-TiO₂:PTA molar ratio of 5:1. Films with varying Sn-TiO₂:PTA molar ratios (3:1, 7:1) were prepared by adjusting precursor quantities. Three independent batches were fabricated for each ratio to ensure reproducibility.

2.1.4. Characterizations

The X-ray powder diffraction (XRD) patterns of the products were performed on a Rigaku SmartLab diffractometer with Cu K α radiation ($\lambda = 1.54178 \text{ \AA}$). Scanning electron microscope (SEM) images were performed on a Hitachi SU8010 microscope. Transmission electron microscopy (TEM) images and elemental mapping results were obtained on Hitachi-7700 and FEI Tecnai G2 F20 microscopes. X-ray photoelectron spectroscopy (XPS) measurement was measured on an Imaging Photoelectron Spectrometer (Escalab 250Xi, Thermo Scientific, Waltham, MA, USA) with a monochromatic Al K α X-ray source. The Fourier transform infrared (FTIR) spectra were conducted on a Bruker Alpha spectrometer in the range of 500–4000 cm^{-1} . UV-vis absorption spectra were measured using a UV-vis spectrophotometer (UV-2600, Shimadzu Co., Tokyo, Japan) equipped with an integrating sphere unit (ISR-2600, Shimadzu Co., Tokyo, Japan). The Raman spectra were recorded on a micro-Raman LabRAM HR800 spectrometer (Horiba Jobin Yvon Ltd., Tokyo, Japan) with a 633 nm laser. Electron spin resonance (ESR) spectrum was measured with a Bruker ESR5000 spectrometer at X-band at 77 K. All photochromic tests were conducted under ambient conditions (temperature: $25 \pm 2 \text{ }^\circ\text{C}$; relative humidity: $50 \pm 5\%$; atmospheric oxygen content: $\sim 21\%$). The digital photographs were obtained by a cellphone.

2.2. Results and Discussion

2.2.1. Synthesis and Structural Characterization of Sn-TiO₂/PTA/PVP Nanocomposite Films

The Sn-TiO₂/PTA/PVP nanocomposite films were synthesized through a hierarchical strategy combining hydrothermal synthesis of Sn-TiO₂ nanoparticles and their subsequent integration with PTA clusters via PVP-mediated interfacial engineering. The structural evolution and chemical interactions within the nanocomposite were systematically investigated using XRD, TEM, FT-IR, XPS, and UV-vis spectroscopy.

The crystalline structure of the synthesized components was first evaluated via XRD. As shown in Figure 1a, pristine Sn-TiO₂ nanoparticles exhibited distinct diffraction peaks at 27.4°, 36.1°, and 54.3°, corresponding to the (100), (101), and (211) planes of the rutile TiO₂ phase (JCPDS No. 21-1276) [38]. Notably, the absence of SnO₂-specific peaks (e.g., $\sim 26.5^\circ$ and $\sim 33.8^\circ$) confirmed that Sn⁴⁺ ions were substitutionally doped into the TiO₂ lattice rather than forming segregated SnO₂ phases [46,47]. This substitutional doping is critical for narrowing the bandgap and enhancing visible-light absorption, as later evidenced by UV-vis analysis. In contrast, the XRD pattern of pristine PTA clusters (H₃PW₁₂O₄₀) displayed sharp peaks at 10.2°, 25.6°, and 34.8°, characteristic of the Keggin-type structure (JCPDS No. 50-0655) [48,49]. The XRD peak broadening observed in the Sn-TiO₂/PTA/PVP nanocomposite film is attributed to the dual functionality of PVP as both a steric stabilizer and a hydrogen-bonding mediator. The pyrrolidone groups within PVP coordinate with Sn-TiO₂ and PTA, disrupting long-range crystallinity and simultaneously enhancing interfacial charge transfer. This observation is supported by FT-IR and XPS data (discussed below), which demonstrate weakened intra-component vibrations (Figure 1g) and electron redistribution (Figure 2a–d).

TEM and SEM images provided insights into the morphology and elemental distribution of the Sn-TiO₂/PTA/PVP nanocomposite film. The TEM image (Figure 1b) revealed that the Sn-TiO₂ nanoparticles exhibited an average size of approximately 5 nm. Figure 1c illustrates the uniform dispersion of Sn-TiO₂ nanoparticles and PTA clusters within the PVP matrix. A digital image (Figure 1d) showed the Sn-TiO₂/PTA/PVP nanocomposite film to be transparent with a yellowish-green color, and the UV-vis transmittance spectrum (Figure S1) indicated a transmittance of approximately 80%. Furthermore, a cross-sectional optical microscope image (Figure 1e) confirmed a film thickness of $\sim 270 \text{ }\mu\text{m}$, while low-magnification SEM (Figure 1f) highlighted a smooth surface morphology with minimal porosity. This dense structure is critical for minimizing oxidative degradation during photochromic cycling by impeding oxygen diffusion into the interior of film. The corresponding elemental mapping (Figure 1f) demonstrated uniform distribution of Sn, Ti, W, P, and N (from PVP) across the nanocomposite film, confirming the absence of agglomeration. The homogeneous elemental distribution underscores the effectiveness of PVP as both a dispersant and interfacial linker, ensuring optimal charge transport pathways [50]. The dual functionality of PVP originates from its pyrrolidone ring, where the carbonyl oxygen (C=O) acts as both a hydrogen bond acceptor and a coordination site. The C=O group forms hydrogen bonds with hydroxylated Sn-TiO₂ surfaces and oxygen-rich PTA clusters, as evidenced by FT-IR peak broadening observed at 1665 cm^{-1} (Figure 1g). Furthermore, coordination between C=O and Ti⁴⁺/Sn⁴⁺ stabilizes Sn-TiO₂ nanoparticles, while electrostatic interactions with PTA anions ensure their uniform dispersion, as depicted in Figure 1f. Complementing these interactions, the hydrophobic polymer backbone provides steric hindrance, effectively preventing agglomeration (Figure 1c). These mechanisms work synergistically to enhance interfacial charge transfer without compromising the structural integrity of the composite.

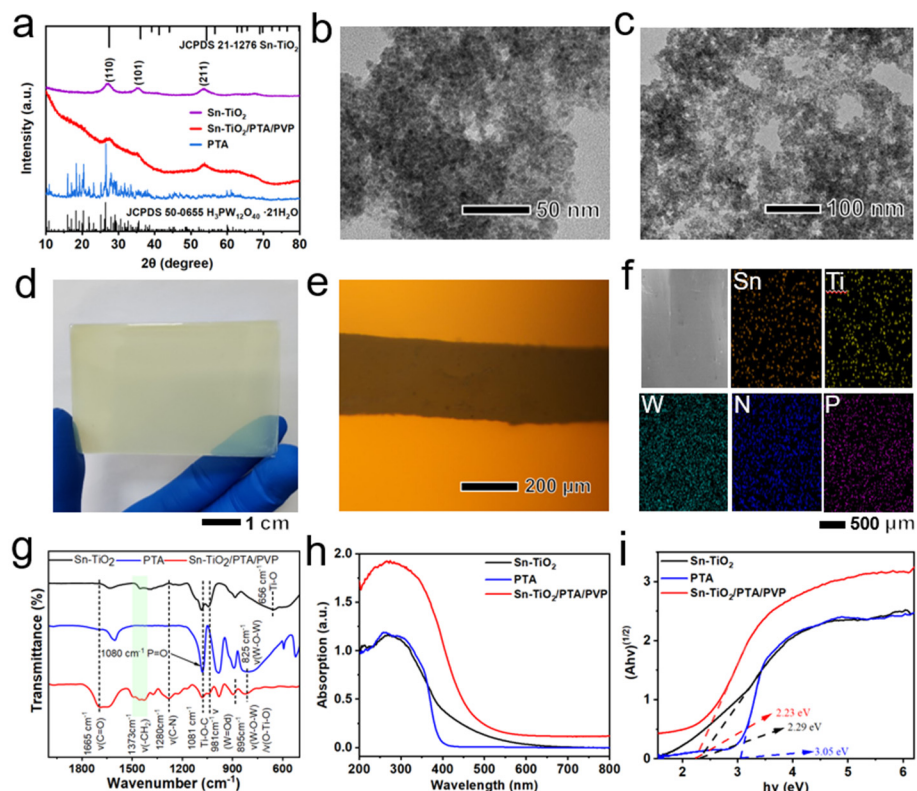


Figure 1. (a) XRD patterns of Sn-TiO₂, PTA, and the typical Sn-TiO₂/PTA/PVP nanocomposite film. (b,c) TEM images of Sn-TiO₂ nanoparticles and the typical Sn-TiO₂/PTA/PVP nanocomposite film. (d) Photograph of the typical Sn-TiO₂/PTA/PVP nanocomposite film. (e) Optical microscope image of the typical Sn-TiO₂/PTA/PVP nanocomposite film from cross-sectional view. (f) SEM images and corresponding elemental mapping of Sn, Ti, W, N, and P of the typical Sn-TiO₂/PTA/PVP nanocomposite film. (g–i) FT-IR spectra, UV–vis diffuse absorption spectra and the corresponding Tauc ((Ahv)^{1/2} versus hv) plots of Sn-TiO₂, PTA, and the typical Sn-TiO₂/PTA/PVP nanocomposite film, respectively.

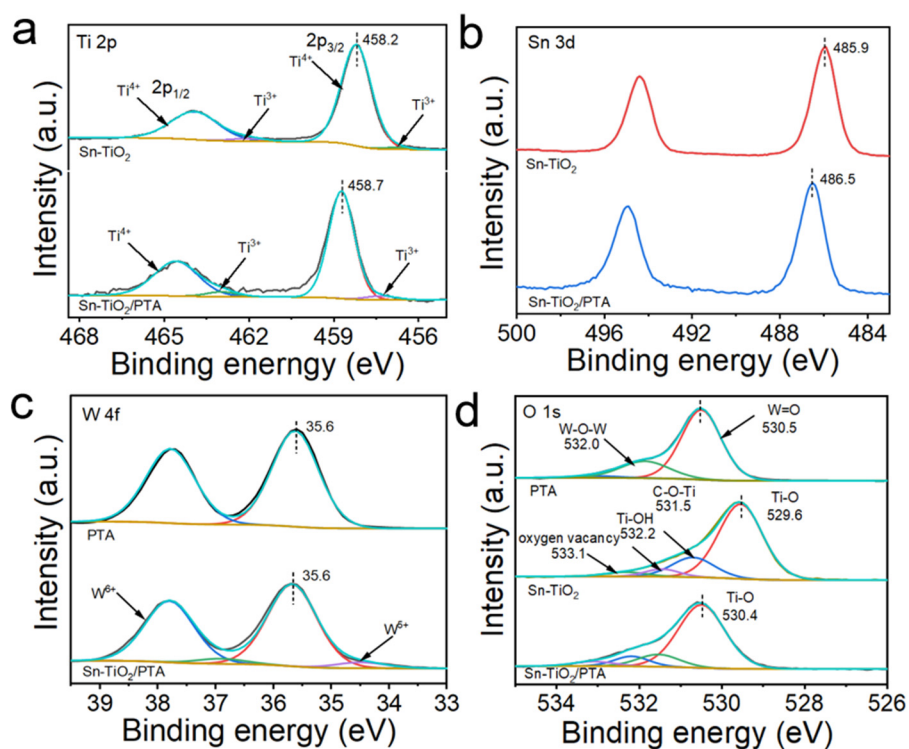


Figure 2. High-resolution XPS spectra of Ti 2p (a), Sn 2p (b), W 4f (c) and O 1s (d) of Sn-TiO₂ nanoparticles, PTA, and Sn-TiO₂/PTA nanocomposite.

Figure 1g shows the FT-IR spectra of Sn-TiO₂, PTA, and the typical Sn-TiO₂/PTA/PVP nanocomposite film (Figures 1g and S2). The peaks at 3605–3412 cm⁻¹ belong to the stretching vibration of O-H bond on the surface of Sn-TiO₂, PTA, and the typical Sn-TiO₂/PTA/PVP nanocomposite. The characteristic peaks at 2856–2928, 1665, 1373, 1280, 1080, 981, 825 and 656 cm⁻¹ arise from the stretching vibration of -CH₂ group, stretching vibration of C=O, wagging vibration of CH₂ group, stretching vibration of the C-N bond, stretching vibration of C-O-Ti or P=O, vibration of W=O, bending vibration of W-O-W, and Ti-O, respectively [39,51,52]. The FT-IR spectra of Sn-TiO₂/PTA/PVP nanocomposite film showed diminished intensity in W-O-W and Ti-O-Ti vibrations (740–525 cm⁻¹), indicative of robust interfacial interactions that suppress nanoparticle aggregation [53,54]. UV-vis diffuse reflectance spectroscopy and Tauc plots (Figure 1h,i) elucidated the optical absorption characteristics and bandgap modulation induced by Sn doping and PVP-mediated integration. The Sn-TiO₂/PTA/PVP nanocomposite exhibited a narrowed bandgap of 2.23 eV, as calculated using Kubelka-Munk function, compared to pristine Sn-TiO₂ (2.29 eV) and PTA (3.05 eV) [55]. Similar bandgap narrowing has been reported for Sn-TiO₂ systems, where Sn⁴⁺ substitution creates defect states that extend visible-light absorption [39]. The broad absorption of the Sn-TiO₂/PTA/PVP nanocomposite film in the 600–800 nm range (Figure 1h) is attributed to IVCT transitions between W⁵⁺ and W⁶⁺ species within the reduced PTA clusters. This IVCT absorption is critical for achieving high-contrast black coloration, as it spans a significant portion of the visible spectrum [56–59]. In contrast, conventional WO₃-based systems exhibit narrower IVCT bands (~600–700 nm), resulting in grayish color [60]. The synergistic effect between the visible-light absorption of Sn-TiO₂ and the broadband IVCT transitions of PTA enables the nanocomposite to achieve enhanced optical contrast.

Due to the shielding effect of the PVP polymer matrix on XPS signals from Sn-TiO₂ and PTA, direct characterization of the photochromic process was performed using Sn-TiO₂/PTA nanocomposites. The survey XPS spectrum (Figure S3) of the Sn-TiO₂/PTA nanocomposite revealed the presence of Ti, Sn, W, P, O, and C signals, originating from the Sn-TiO₂ nanoparticles and PTA components. High-resolution XPS analysis revealed critical insights into interfacial charge transfer dynamics. The Ti 2p_{3/2} core-level spectrum (Figure 2a) exhibited a binding energy shift from 458.2 eV (pristine Sn-TiO₂) to 458.7 eV in the nanocomposite, while the Sn 3d_{5/2} peak shifted from 485.9 eV to 486.5 eV (Figure 2b). These upward shifts indicate electron depletion at Ti and Sn sites, suggesting electron transfer from Sn-TiO₂ to adjacent species. Conversely, the O 1s peak shifted downward by 0.1 eV (from 530.5 eV in pristine PTA to 530.4 eV in the nanocomposite; Figure 2d), reflecting increased electron density on oxygen atoms, likely due to electron accumulation from Sn-TiO₂ [61,62]. Notably, the W 4f spectra remained unchanged, ruling out direct involvement of W redox states in the interfacial charge transfer process (Figure 2c). The directional electron flow aligns with the observed photochromic kinetics (discussed later), where Sn-TiO₂ acts as an electron donor under visible light, reducing PTA and triggering IVCT transitions. This mechanism is further corroborated by the stability of W 4f signals, which confirms that PTA maintains its structural integrity during charge transfer, serving as a robust electron acceptor. By excluding PVP, this analysis isolates the intrinsic interactions between Sn-TiO₂ and PTA, clarifying their synergistic roles in photochromic behavior.

2.2.2. Photochromic Performance of Sn-TiO₂/PTA/PVP Nanocomposite Films

The photochromic behavior of the Sn-TiO₂/PTA/PVP nanocomposite films was systematically evaluated under 450 nm illumination and H₂O₂ vapor treatment, with a focus on coloration kinetics, bleaching dynamics, cyclic stability, and component ratio effects. For the optimal Sn-TiO₂:PTA molar ratio (5:1), the film exhibited ultrafast coloration within 10 s (Figure 3a), achieving a maximum absorbance at 750 nm (Figure 3b). Illumination with 450 nm light resulted in a pronounced color change in the nanocomposite film, transitioning from an initial light yellow to a black color. This color change is indicative of efficient electron transfer from the Sn-TiO₂ nanoparticles to the PTA component (Figure 3a). Concurrently, the UV-vis diffuse reflectance spectra of the Sn-TiO₂/PTA/PVP nanocomposite film exhibited a time-dependent increase in absorption across the visible region (470–800 nm) upon exposure to 450 nm light for 10 s, with a characteristic absorption peak observed at 750 nm (Figure 3b). This absorption peak is attributed to IVCT transition between W⁵⁺ and W⁶⁺ species, providing direct evidence for the reduction of W⁶⁺ to W⁵⁺ within the nanocomposite film under 450 nm illumination [31]. The bleaching kinetics of the Sn-TiO₂/PTA/PVP nanocomposite film were initially investigated under ambient atmospheric conditions (Figure 3c). The UV-vis diffuse reflectance spectrum of the photoreduced (darkened) film revealed a gradual decrease in absorption intensity as a function of time, which is attributed to the slow reoxidation kinetics of W⁵⁺ back to W⁶⁺ by molecular oxygen present in the ambient air [61]. Beyond 50 h, no further decrease in the UV-vis diffuse reflectance intensity was observed, suggesting that oxygen diffusion from the surface to the interior of the film becomes diffusion-limited due to PVP's oxygen-blocking effect. The prolonged color retention of the photoreduced Sn-TiO₂/PTA/PVP nanocomposite film, lasting for more than 2 days, renders this system a

promising candidate for rewritable paper applications. In order to further manipulate and accelerate the bleaching process for potential applications, the nanocomposite film was subjected to treatment with H₂O₂ vapor. As depicted in Figure 3d, the UV–vis diffuse reflectance spectra of the photoreduced (darkened) film exhibited a gradual shift towards the reverse direction, with complete recovery to the initial state achieved within a period of 22 min upon exposure to H₂O₂ vapor (3 wt. %). This rapid bleaching is attributed to the efficient oxidation of W⁵⁺ back to W⁶⁺ within the Sn-TiO₂/PTA/PVP nanocomposite film, where H₂O₂ acts as an effective oxidizing agent [62]. The resulting H₂O₂-treated film demonstrated an enhanced bleaching rate (Figure 3e). The coloration and bleaching process, induced by illumination with 450 nm light and subsequent treatment with 3 wt.% H₂O₂ vapor, respectively, was repeated multiple times to investigate the reversibility and stability of the Sn-TiO₂/PTA/PVP nanocomposite film for potential applications (Figure 3f). The UV-Vis diffuse reflectance spectra were acquired, and the intensity at 750 nm was monitored to quantify the coloration and bleaching efficiency. The nanocomposite film demonstrated exceptional photochromic reversibility and repeatability, retaining over 95% of its initial absorbance after 80 cycles. The performance of the Sn-TiO₂/PTA/PVP nanocomposite film surpasses that of many existing photochromic systems, as detailed in Table S1.

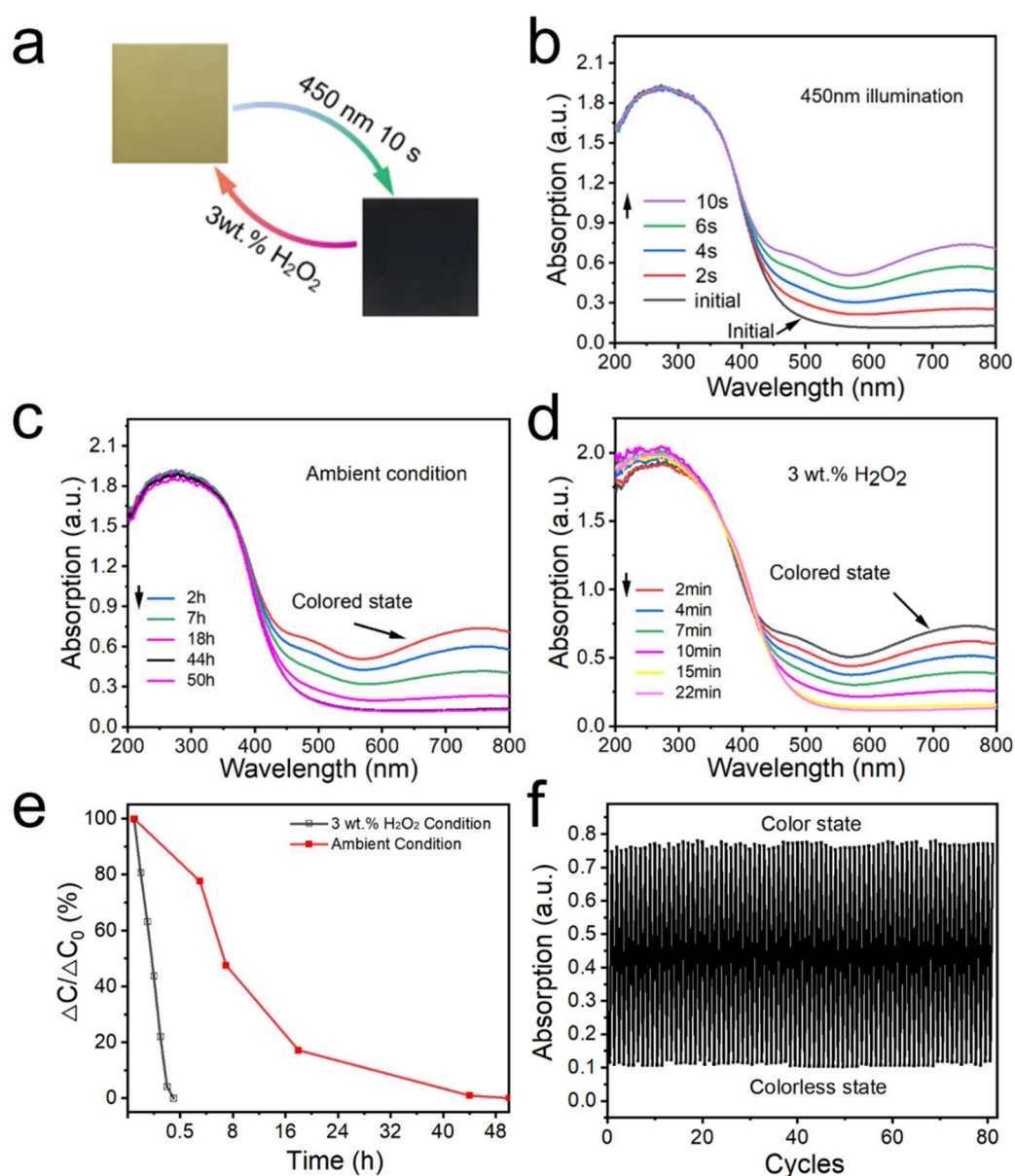


Figure 3. (a) Digital photographs showing the color switching process of the typical Sn-TiO₂/PTA/PVP nanocomposite film upon 450 nm illumination and treatment with H₂O₂ vapor. (b–d) UV-vis diffuse absorption spectra showing the coloration process upon 450 nm illumination (b), upon the bleaching process in ambient air (c), and in the 3 wt.% H₂O₂ condition (d). (e) The bleaching rate of the Sn-TiO₂/PTA/PVP nanocomposite film in the ambient condition and treated with H₂O₂ vapor, respectively. (f) Absorption intensity at 750 nm of the nanocomposite film in 80 cycles.

To further elucidate the impact of component ratios, the photochromic performance of Sn-TiO₂/PTA/PVP nanocomposite films with Sn-TiO₂:PTA molar ratios of 3:1 and 7:1 was also investigated, respectively. While the 3:1 ratio nanocomposite film exhibited a noticeable color change from light gray to black upon 10 s of illumination with 450 nm light, its cycling stability was limited to only 50 cycles (Figures S4 and S6a). This limited stability at the 3:1 Sn-TiO₂:PTA ratio can be attributed to the lower Sn-TiO₂ content, which restricts the number of photogenerated electrons available for PTA reduction. Consequently, the reduction of W⁶⁺ to W⁵⁺ is slowed due to this insufficient electron density, leading to incomplete coloration and accelerated degradation of the partially reduced PTA clusters during cycling. Conversely, the 7:1 ratio resulted in excessive aggregation of Sn-TiO₂ nanoparticles, which hindered film formation. Consequently, the 7:1 ratio nanocomposite film displayed minimal color change after 10 s of illumination at 450 nm (Figures S5 and S6b). These findings highlight the critical importance of maintaining balanced component ratios to achieve optimal photochromic performance.

2.2.3. Mechanistic Insights into Photochromic Behavior

The photochromic mechanism of the Sn-TiO₂/PTA nanocomposite was elucidated through XPS and FTIR analyses. Upon 450 nm illumination, this peak of W 4f_{7/2} peak shifted from 35.6 eV to 35.4 eV (Figure 4a), confirming the reduction of W⁶⁺ to W⁵⁺ [58]. The intensity ratio of W⁵⁺/W⁶⁺ increased after illumination, indicating efficient electron accumulation at PTA clusters. Concurrently, the Ti 2p_{3/2} peak shifted from 458.7 eV to 458.5 eV (Figure 4b), signifying the formation of Ti³⁺ species via electron trapping at oxygen vacancies [31]. These vacancies, introduced by Sn⁴⁺ substitution into the TiO₂ lattice, act as hole scavengers, prolonging electron lifetimes (>10 ns) and enhancing charge separation efficiency [38]. The O 1s peak shifted downward by 0.2 eV (from 530.5 to 530.3 eV; Figure 4c), reflecting increased electron density at oxygen sites due to interfacial charge transfer. These observations align with prior studies on metal oxide-POM systems, where visible-light excitation drives directional electron flow from the semiconductor to POM clusters [31]. The survey XPS spectra (Figure S7) confirmed the absence of elemental leaching or phase decomposition during cycling, with C 1s and P 2p peaks remaining unchanged, underscoring the structural integrity of the Sn-TiO₂ and PTA clusters.

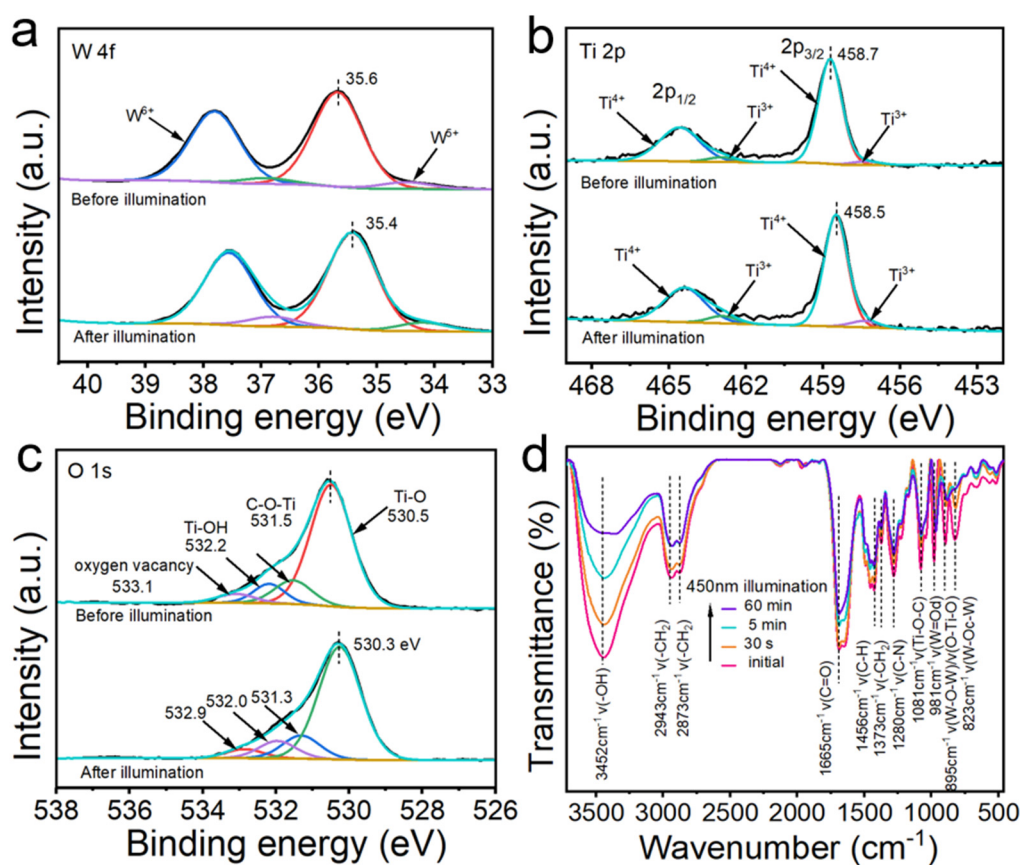


Figure 4. (a,b) High-resolution XPS spectra of W 4f (a), Ti 2p (b) and O 1s (c) of the Sn-TiO₂/PTA nanocomposite before and after 450 nm illumination. (d) FT-IR spectra of the Sn-TiO₂/PTA/PVP nanocomposite film upon 450 nm with different time.

FT-IR spectroscopy (Figure 4d) provided further evidence of dynamic interfacial interactions during photochromic cycling. The W–O–W vibrational peak at 895 cm⁻¹ decreased in intensity within 30 s of illumination, indicating electron localization at W sites. Simultaneously, the –OH vibrational peak at 3452 cm⁻¹ exhibited a sharp intensity decline with prolonged illumination, attributed to hydroxyl group formation via water oxidation by photogenerated holes. This process stabilizes charge-separated states by suppressing hole recombination [63,64]. The W=O stretching vibration at 981 cm⁻¹ also diminished, suggesting partial reduction of terminal oxygen atoms in PTA. These spectral changes correlate with enhanced interfacial electronic coupling between Sn-TiO₂ and PTA, facilitating unidirectional electron transfer under visible light. Notably, the C–N vibrational peak of PVP (1280 cm⁻¹) remained almost unchanged during illumination, confirming its non-redox role as a structural stabilizer. PVP suppresses nanoparticle aggregation and oxidative degradation by forming a protective matrix, ensuring uniform dispersion of Sn-TiO₂ and PTA clusters.

2.2.4. Application of Sn-TiO₂/PTA/PVP Nanocomposite Films as Rewritable Smart Media

The practical utility of the Sn-TiO₂/PTA/PVP nanocomposite film as a high-performance rewritable medium was demonstrated through photopatterning experiments and environmental stability tests, as illustrated in Figure 5. Leveraging its ultrafast visible-light-driven photochromism, high optical contrast, and robust reversibility, the film enables precise, durable, and eco-friendly information recording and erasing, addressing critical limitations of conventional rewritable systems. As shown in Figure 5a, high-definition text patterns were printed onto the nanocomposite film using 450 nm illumination through a photomask (10 s exposure). The printed patterns exhibited sharp edge definition and no pixel bleeding, demonstrating the localized photochromism of the material. This spatial selectivity arises from efficient electron transfer from Sn-TiO₂ to PTA exclusively in illuminated regions, triggering W⁶⁺-to-W⁵⁺ reduction and subsequent broadband IVCT absorption. The environmental stability of printed information was assessed under ambient conditions. As illustrated in Figure 5b, legible text remained discernible for up to 3 days, with complete disappearance observed after 6 days (Figure 5b, panels i–vi). This extended retention time represents a significant improvement compared to organic dye-based systems, such as spiropyran, which typically exhibit a retention period of less than 3 days [65]. This performance characteristic aligns well with the requirements for temporary display applications in logistics, signage, and anti-counterfeiting labels. The slow oxidative fading is attributed to the dense PVP matrix, which impedes oxygen diffusion into the film's interior.

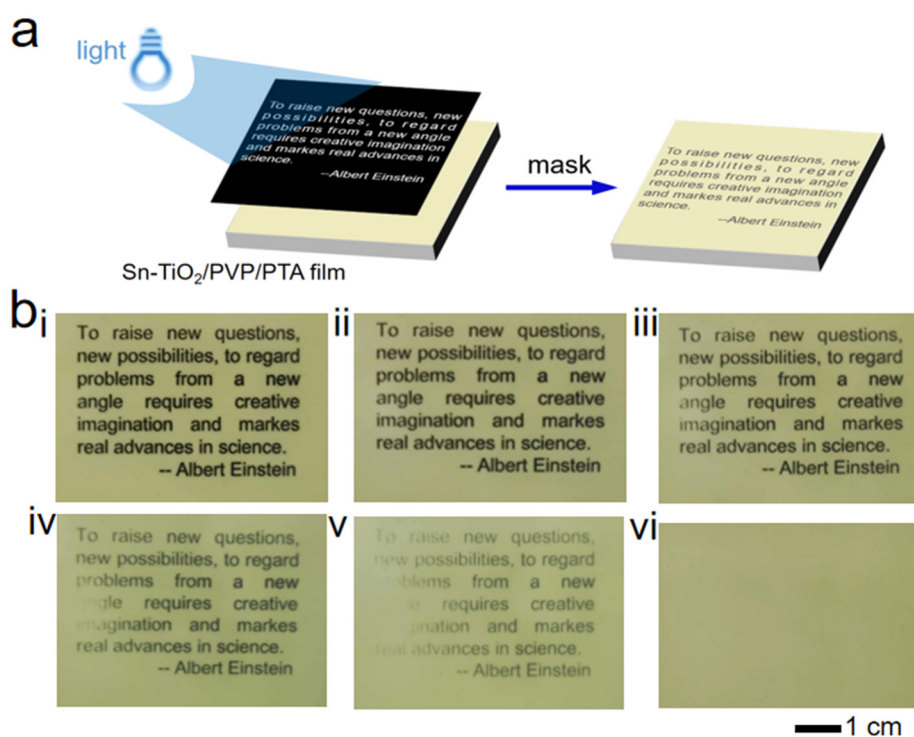


Figure 5. (a) Schematic illustration of photoprinting on the Sn-TiO₂/PTA/PVP nanocomposite film under 450 nm illumination in 10 s using a photomask. (b) Digital photographs of the original printed rewritable film (i) and the printed rewritable film maintained in air for 6 h (ii), 12 h (iii), 2 days (iv), 3 days (v), 6 days (vi).

3. Conclusions

In summary, we present a visible-light-responsive Sn-TiO₂/PTA/PVP nanocomposite film that synergizes ultrafast photochromic switching, high-contrast black coloration, and exceptional environmental stability for rewritable media applications. By leveraging Sn⁴⁺ doping to narrow the TiO₂ bandgap (2.23 eV) and PVP-mediated interfacial engineering to integrate PTA clusters, the nanocomposite achieves efficient visible-light absorption (400–500 nm) and broadband IVCT transitions (600–800 nm), enabling full-spectrum black coloration. The material exhibits ultrafast coloration (10 s under 450 nm illumination) and rapid bleaching (<30 min via H₂O₂ vapor), sustaining over 80 reversible cycles with negligible performance decay. This represents a significant improvement over organic dyes and UV-dependent inorganic systems in terms of both speed and durability. The dense PVP matrix further ensures long-term stability by suppressing oxidative degradation, retaining legible patterns for >48 h under ambient conditions. As a rewritable smart medium, the film enables high-resolution, energy-efficient information storage and erasure, showcasing direct applicability in temporary displays, smart packaging, and dynamic signage. From an environmental perspective, the Sn-TiO₂/PTA/PVP nanocomposite offers a sustainable alternative to conventional photochromic systems. The inorganic components (Sn-TiO₂, PTA) are non-toxic and abundant, while the aqueous synthesis process avoids hazardous solvents. The visible-light-driven mechanism reduces energy consumption compared to UV-dependent systems, and the film's long-term stability (>80 cycles) minimizes material waste. These attributes align with global efforts toward green chemistry and energy-efficient technologies. By harmonizing visible-light activation, high optical contrast, and mechanical durability within an eco-friendly inorganic framework, this work establishes a transformative platform for next-generation smart displays, anti-counterfeiting technologies, and energy-efficient rewritable media.

Supplementary Materials: The following supporting information can be downloaded at: <https://media.scilitp.com/articles/others/2505151554522574/MI-953-SI-final.pdf>, Figure S1: UV-vis transmittance spectrum of the typical Sn-TiO₂/PTA/PVP nanocomposite film; Figure S2: FT-IR spectra of Sn-TiO₂, PTA, and the typical Sn-TiO₂/PTA/PVP nanocomposite film; Figure S3: Survey XPS spectra (a) and high-resolution XPS spectra of C 1s (b) and P 2p (d) of PTA, Sn-TiO₂ nanoparticles and Sn-TiO₂/PTA nanocomposite; Figure S4: (a) Digital photographs showing the color switching process of the Sn-TiO₂/PTA/PVP nanocomposite film (the molar ratio of Sn-TiO₂:PTA is 3:1) upon 450 nm illumination and treatment with H₂O₂ vapor. (b,c) UV-vis diffuse absorption spectra showing the coloration process upon 450 nm illumination (b), upon the bleaching process in the 3 wt.% H₂O₂ condition (c); Figure S5: (a) Digital photographs showing the color switching process of the Sn-TiO₂/PTA/PVP nanocomposite (the molar ratio of Sn-TiO₂:PTA is 7:1) upon 450 nm illumination and treatment with H₂O₂ vapor. (b,c) UV-vis diffuse absorption spectra showing the coloration process upon 450 nm illumination (b), upon the bleaching process in the 3 wt.% H₂O₂ condition (c); Figure S6: (a) The coloration rate and (b) the bleaching rate of Sn-TiO₂/PTA/PVP nanocomposite films with different Sn-TiO₂:PTA molar ratios under 450 nm light illumination in the initial state, treatment with vapor of H₂O₂, respectively. (c) Absorption intensity at 750 nm of films with Sn-TiO₂:PTA molar ratios of 5:1 (80 cycles) and 3:1 (50 cycles) during continuous color switching. Figure S7: Survey XPS spectra (a) and high-resolution XPS spectra of C (b), P (c), N (d) of the Sn-TiO₂/PTA nanocomposite before and after 450 nm illumination. Table S1: Comparison of photochromic performance between Sn-TiO₂/PTA/PVP and existing systems. References [66–69] are cited in the supplementary materials.

Author Contributions: Y.D: conceptualization, methodology, software; D.W: data curation, writing—original draft preparation; Y.Q.: visualization, investigation; Y.Z.: supervision; Z.Z.: software, validation; W.W.: writing—reviewing and editing. All authors have read and agreed to the published version of the manuscript.

Funding: This work was supported by the Natural Science Foundation of Shandong Province (ZR2019JQ15, ZR2024QB097), National Natural Science Foundation of China (22479063), and University of Jinan Postdoctoral Initiation Fund (No.1003880).

Data Availability Statement: The data presented in this study are available upon request from the corresponding author.

Conflicts of Interest: The authors declare no conflict of interest.

References

1. Ke, Y.; Chen, J.; Lin, G.; Wang, S.; Zhou, Y.; Yin, J.; Lee, P.S.; Long, Y. Smart Windows: Electro-, Thermo-, Mechano-, Photochromics, and Beyond. *Adv. Energy Mater.* **2019**, *9*, 1902066.
2. Chun, S.Y.; Park, S.; Lee, S.I.; Nguyen, H.D.; Lee, K.-K.; Hong, S.; Han, C.-H.; Cho, M.; Choi, H.-K.; Kwak, K. Operando Raman and UV-Vis spectroscopic investigation of the coloring and bleaching mechanism of self-powered photochromic devices for smart windows. *Nano Energy* **2021**, *82*, 105721.
3. Pang, Q.; Bian, L.; Xu, J.; Jia, Y.; Wang, C.; Zhang, Y.; Ju, Q.; Wu, Q.; Fang, Z. Sunlight-Sensitizing Switchable Photochromic Transparent Aesthetic Wood for Smart Windows. *ACS Sustain. Chem. Eng.* **2024**, *12*, 10506–10516.
4. Meng, W.; Kragt, A.J.J.; Gao, Y.; Brembilla, E.; Hu, X.; van der Burgt, J.S.; Schenning, A.; Klein, T.; Zhou, G.; van den Ham, E.R.; et al. Scalable Photochromic Film for Solar Heat and Daylight Management. *Adv. Mater.* **2024**, *36*, e2304910.
5. Ma, T.; Li, B.; Zhu, Y.; Wu, S.; Zhao, X.; Chu, X.; Tian, S. Enhanced photochromic performance of Zn-doped W₁₈O₄₉-based films for smart windows. *J. Mater. Chem. C* **2024**, *12*, 10218–10225.

6. Sheng, L.; Li, M.; Zhu, S.; Li, H.; Xi, G.; Li, Y.G.; Wang, Y.; Li, Q.; Liang, S.; Zhong, K.; et al. Hydrochromic molecular switches for water-jet rewritable paper. *Nat. Commun.* **2014**, *5*, 3044.
7. Smith, A.T.; Ding, H.; Gorski, A.; Zhang, M.; Gitman, P.A.; Park, C.; Hao, Z.; Jiang, Y.; Williams, B.L.; Zeng, S.; et al. Multi-color Reversible Photochromisms via Tunable Light-Dependent Responses. *Matter* **2020**, *2*, 680–696.
8. Sarker, S.; Macharia, D.K.; Zhang, Y.; Zhu, Y.; Li, X.; Wen, M.; Meng, R.; Yu, N.; Chen, Z.; Zhu, M. Synthesis of MnO₂-Ag Nanojunctions with Plasmon-Enhanced Photocatalytic and Photothermal Effects for Constructing Rewritable Mono-/Multi-Color Fabrics. *ACS Appl. Mater. Interfaces* **2022**, *14*, 5545–5557.
9. Wang, W.; Yi, L.; Zheng, Y.; Lu, J.; Jiang, A.; Wang, D. Photochromic and mechanochromic cotton fabric for flexible rewritable media based on acrylate latex with spiropyran cross-linker. *Compos. Commun.* **2023**, *37*, 101455.
10. Cui, B.; Guo, C.; Zhang, Z.; Fu, G. Core-shell ZnCo-PBA@WO_{2.72} heterojunctions with enhanced photo-responsive color switching ability for highly efficient rewritable media and information encryption. *Chem. Eng. J.* **2023**, *477*, 147037.
11. Zhang, J.; Guo, M.; Su, Y.; Wu, W.; Wang, S.; Yang, R.; Xu, C.; Yin, H.; Xu, J.; Wang, X. Photochromic ionogel with a wide temperature range and fatigue resistance for high-resolution rewritable information record. *Chem. Eng. J.* **2024**, *495*, 153263.
12. Chen, T.; Xu, B.; Han, J.; Zhu, M.; Zhang, J.; Li, Z. Chelating Coordination Regulated Photochromic Electrospun Nanofibers for Waterproof and Long-Color-Retention Rewritable Wearables. *ACS Appl. Mater. Interfaces* **2024**, *16*, 13305–13315.
13. Li, P.; Zhang, Z.; Gao, X.; Sun, H.; Peng, D.; Zou, H.; Zhang, Q.; Hao, X. Fast self-bleaching Nb₂O₅-based photochromics for high security dynamic anti-counterfeiting and optical storage applications. *Chem. Eng. J.* **2022**, *435*, 134801.
14. Li, X.; Lin, H.; Lin, S.; Li, P.; Wang, P.; Xu, J.; Cheng, Y.; Zhang, Q.; Wang, Y. Rare-Earth-Ion Doped Bi_{1.5}ZnNb_{1.5}O₇ Photochromics: A Fast Self-Recoverable Optical Storage Medium for Dynamic Anti-Counterfeiting with High Security. *Laser Photonics Rev.* **2023**, *17*, 2200734.
15. Wan, J.; Xu, J.; Zhu, S.; Li, J.; Chen, K. Multicolor photochromic material with dual protection of anti-counterfeiting and waterproofing. *Chem. Eng. J.* **2023**, *473*, 145500.
16. Sun, L.; Wang, B.; Xing, G.; Liang, C.; Ma, W.; Yang, S. Bi-induced photochromism and photo-stimulated luminescence with fast photochromic response for multi-mode dynamic anti-counterfeiting and optical information storage. *Chem. Eng. J.* **2023**, *455*, 140752.
17. Hu, L.; Gao, Y.; Cai, Q.; Wei, Y.; Zhu, J.; Wu, W.; Yang, Y. Cholesterol-substituted spiropyran: Photochromism, thermochromism, mechanochromism and its application in time-resolved information encryption. *J. Colloid Interface Sci.* **2024**, *665*, 545–553.
18. Wang, L.; Zhong, W.; Gao, W.; Liu, W.; Shang, L. Dynamic multicolor luminescent anti-counterfeiting based on spiropyran-engineered gold nanoclusters. *Chem. Eng. J.* **2024**, *479*, 147490.
19. Song, Y.; Zhao, Y.; Huang, Z.; Zhao, J. Aqueous synthesis of molybdenum trioxide (h-MoO₃, α-MoO₃·H₂O and h-/α-MoO₃ composites) and their photochromic properties study. *J. Alloys Compd.* **2017**, *693*, 1290–1296.
20. Wang, W.; Ye, Y.; Feng, J.; Chi, M.; Guo, J.; Yin, Y. Enhanced photoreversible color switching of redox dyes catalyzed by barium-doped TiO₂ nanocrystals. *Angew. Chem. Int. Ed.* **2015**, *54*, 1321–1326.
21. Kozlov, D.A.; Shcherbakov, A.B.; Kozlova, T.O.; Angelov, B.; Kopitsa, G.P.; Garshev, A.V.; Baranchikov, A.E.; Ivanova, O.S.; Ivanov, V.K. Photochromic and Photocatalytic Properties of Ultra-Small PVP-Stabilized WO₃ Nanoparticles. *Molecules* **2019**, *25*, 154.
22. Yan, X.; Zhong, W.; Qu, S.; Li, Z.; Shang, L. Photochromic Tungsten Oxide Quantum Dots-based Fluorescent Photoswitches towards Dual-mode Anti-counterfeiting Application. *J. Colloid Interface Sci.* **2023**, *646*, 855–862.
23. Wang, F.; Song, Y.; Xie, R.; Li, J.; Zhang, X.; Xie, H.; Zou, H. TiO₂/PVA Based Composites: Visible Light Activated Rapid Dual-Mode optical Response. *Chem. Eng. J.* **2023**, *475*, 146306.
24. Li, L.; Yu, Y.-T.; Zhang, N.-N.; Li, S.-H.; Zeng, J.-G.; Hua, Y.; Zhang, H. Polyoxometalate (POM)-based crystalline hybrid photochromic materials. *Coord. Chem. Rev.* **2024**, *500*, 215526.
25. Zhang, J.; Chen, T.; Zhu, M.; Lu, J.; Liu, X.; Sun, W.; So, M.Y.; Xu, B. Scalable, Fast Light-Responsive, and Excellent Color-Retention Fiber-Based Photochromic Wearables for Sustainable Photo-Patterning and Information Security Encryption. *Adv. Funct. Mater.* **2024**, *35*, 2415622.
26. Pope, T.R.; Lassig, M.N.; Neher, G.; Weimar Iii, R.D.; Salguero, T.T. Chromism of Bi₂WO₆ in single crystal and nanosheet forms. *J. Mater. Chem. C* **2014**, *2*, 3223–3230.
27. Kayani, A.B.A.; Kuriakose, S.; Monshipouri, M.; Khalid, F.A.; Walia, S.; Sriram, S.; Bhaskaran, M. UV Photochromism in Transition Metal Oxides and Hybrid Materials. *Small* **2021**, *17*, e2100621.
28. Yang, Y.; Li, J.; Li, X.; Guan, L.; Gao, Z.; Duan, L.; Jia, F.; Gao, G. Easily Prepared and Reusable Films for Fast-Response Rewritable Light Printing. *ACS Appl. Mater. Interfaces* **2019**, *11*, 14322–14328.
29. Wu, W.; Ni, M.; Feng, Q.; Zhou, Y.; Cui, Y.; Zhang, Y.; Xu, S.; Lin, L.; Zhou, M.; Li, Z. A wet bacterial cellulose film self-anchored by phosphotungstic acid: Flexible, quick-response and stable cycling performance for photochromic

- application. *Mater. Des.* **2024**, *238*, 112613.
30. Hussain, M.; Ahmad, Z.; Ejeromedoghene, O.; Shehzad, K.; Akhtar, M.; Fu, G. Hybrid polysaccharide film infused with polyoxometalates for inkless printing and solar ultraviolet sensing. *Int. J. Biol. Macromol.* **2025**, *293*, 139308.
 31. Zhang, Y.; Gao, Z.; Liu, F.; Liu, L.; Yan, M.; Wang, W. Electrostatic Assembly of Photochromic TiO₂/Phosphomolybdic Acid Composite Nanoparticles for Light-Responsive Rewritable Papers. *ACS Appl. Nano Mater.* **2022**, *5*, 13218–13226.
 32. Tian, Y.; Liu, W.; Hu, J.; Li, Z.; Xin, X.; Fu, G. Synthesis of highly transparent and fast-responding photochromic coating by template method with space-limited domains. *Chem. Eng. J.* **2024**, *500*, 156961.
 33. Hutomo, F.A.; Pramata, A.D.; Saputra, F.; Pratama, P.R.; De Yonarosa, T.G.; Rasyida, A.; Widyastuti; Sutarsis; Hamidah, N.L. Visible light-driven Synergistic antimicrobial activity of Cu₂O quantum dots and electrospun PAN/PCL nanofiber matrix. *J. Sci.:Adv. Mater. Devices* **2024**, *9*, 100779.
 34. Nazari, S.; Asgari, E.; Sheikhmohammadi, A.; Mokhtari, S.A.; Alamgholiloo, H. Visible-light-driven photocatalytic activity of WO₃/ZIF-67 S-scheme heterojunction for upgrading degradation of oxytetracycline. *J. Environ. Chem. Eng.* **2023**, *11*, 110393.
 35. Jia, L.; Ma, N.; Shao, P.; Ge, Y.; Liu, J.; Dong, W.; Song, H.; Lu, C.; Zhou, Y.; Xu, X. Incorporating ReS₂ Nanosheet into ZnIn₂S₄ Nanoflower as Synergistic Z-Scheme Photocatalyst for Highly Effective and Stable Visible-Light-Driven Photocatalytic Hydrogen Evolution and Degradation. *Small* **2024**, *20*, e2404622.
 36. Zhang, J.; Lei, Y.; Jiang, J.; Zhao, S.; Yi, H.; Tang, X.; Huang, X.; Zhou, Y.; Gao, F. ZnIn₂S₄/g-C₃N₄ binary heterojunction nanostructure for enhancing visible light CO₂ reduction at the reaction interface. *Renew. Energy* **2025**, *242*, 122380.
 37. Chen, P.; Wang, X.; Liu, B.; Yan, L.; Du, X.; Zhang, J.; Zhao, J. Cu-doped KTN crystal with controllable, reversible, and fast photochromic properties: A superior electro-optical material for improving beam deflection performance. *Ceram. Int.* **2024**, *50*, 32645–32654.
 38. Wang, B.; Guo, Y.; Li, Q.; Xin, C.; Tian, Y.; Zhang, W.; Yu, X. Design of porous ZrO₂ with well-tuned band structures and strong visible-light harvesting via Zn doping for enhanced visible-light photocatalysis. *Chem. Eng. J.* **2024**, *481*, 148489.
 39. Zhang, Y.; Dou, Y.; Ye, Z.; Xue, W.; Liu, F.; Yan, M.; Wang, W.; Yin, Y. Visible-Light-Responsive Photoreversible Multi-Color Switching for Rewritable Light-Printing and Information Display. *Small* **2024**, *20*, e2310962.
 40. Ma, Y.; Li, A.; Wang, C.; Ge, X. Preparation of HPW@UiO-66 catalyst with defects and its application in oxidative desulfurization. *Chem. Eng. J.* **2021**, *404*, 127062.
 41. Sun, A.; Nan, F.; Wei, Q.; Wang, L.; Yu, W.W. Color-tunable, multifunctional photochromic composites for wearable UV monitoring and biomechanical energy harvesting. *Nano Energy* **2024**, *126*, 109679.
 42. Xiong, T.; Yong, W.; Chen, N.; Fu, G. Transparent insulating photochromic PU/PTA films for Wide-Spectrum modulated smart windows. *J. Photochem. Photobiol. A* **2024**, *456*, 115853.
 43. Gu, H.; Guo, C.; Zhang, S.; Bi, L.; Li, T.; Sun, T.; Liu, S. Highly Efficient, Near-Infrared and Visible Light Modulated Electrochromic Devices Based on Polyoxometalates and W₁₈O₄₉ Nanowires. *ACS Nano* **2018**, *12*, 559–567.
 44. Chen, L.; Chen, W.L.; Wang, X.L.; Li, Y.G.; Su, Z.M.; Wang, E.B. Polyoxometalates in dye-sensitized solar cells. *Chem. Soc. Rev.* **2019**, *48*, 260–284.
 45. Chen, X.; Zhang, G.; Li, B.; Wu, L. An integrated giant polyoxometalate complex for photothermally enhanced catalytic oxidation. *Sci. Adv.* **2021**, *7*, eabf8413.
 46. Ganeshraja, A.S.; Thirumurugan, S.; Rajkumar, K.; Zhu, K.; Wang, Y.; Anbalagan, K.; Wang, J. Effects of structural, optical and ferromagnetic states on the photocatalytic activities of Sn–TiO₂ nanocrystals. *RSC Adv.* **2016**, *6*, 409–421.
 47. Xiang, H.; Luo, T.; Ji, Y.; Xiong, T.; Qian, L.; Yang, S.; Wang, H. Photocatalytic degradation of low-concentration gaseous benzene in air via bifunctional tin-doped titanium dioxide catalyst. *Environ. Technol. Innov.* **2024**, *36*, 103804.
 48. Cui, Y.; Xing, Z.; Guo, M.; Qiu, Y.; Fang, B.; Li, Z.; Wang, Y.; Chen, P.; Zhou, W. Core-shell carbon colloid sphere@phosphotungstic acid/CdS as a Z-scheme heterojunction with synergistic adsorption, photothermal and photocatalytic performance. *Catal. Sci. Technol.* **2021**, *11*, 6080–6088.
 49. Cai, S.; Wu, H.; Gao, X.; Chen, X.; Cheng, C.; Yang, X.; Sun, R. Phosphotungstic acid decorated free-standing electrode accelerates polysulfides conversion for high-performance flexible Li-S batteries. *J. Energy Storage* **2024**, *89*, 111663.
 50. Li, R.; Zhou, Y.; Shao, Z.; Zhao, S.; Chang, T.; Huang, A.; Li, N.; Ji, S.; Jin, P. Enhanced Coloration/Bleaching Photochromic Performance of WO₃ Based on PVP/PU Composite Matrix. *Chem. Select* **2019**, *4*, 9817–9821.
 51. Yang, Z.; Wang, D.; Zhang, Y.; Feng, Z.; Liu, L.; Wang, W. Photoreductive BiOCl ultrathin nanosheets for highly efficient photocatalytic color switching. *ACS Appl. Mater. Interfaces* **2020**, *12*, 8604–8613.
 52. Gao, Z.; Zhou, Z.; Wang, M.; Shang, N.; Gao, W.; Cheng, X.; Gao, S.; Gao, Y.; Wang, C. Highly dispersed Pd anchored on heteropolyacid modified ZrO₂ for high efficient hydrodeoxygenation of lignin-derivatives. *Fuel* **2023**, *334*, 126768.
 53. Boga, B.; Székely, I.; Pap, Z.; Baia, L.; Baia, M. Detailed Spectroscopic and Structural Analysis of TiO₂/WO₃ Composite Semiconductors. *J. Spectro.* **2018**, *2018*, 6260458.
 54. Khan, H.; Rigamonti, M.G.; Boffito, D.C. Enhanced photocatalytic activity of Pt-TiO₂/WO₃ hybrid material with energy storage ability. *Appl. Catal. B* **2019**, *252*, 77–85.

55. Wei, D.; Zhang, Y.; Xue, W.; Dou, Y.; Liu, F.; Yan, M.; Wang, W. Visible-Light-Responsive Photoreversible Color Switching of Oxygen-Deficient WO_{3-x} Hierarchical Nanostructures for Long-Legible Rewritable Paper. *ACS Sustain. Chem. Eng.* **2024**, *12*, 6310–6319.
56. Hua, C.; Doheny, P.W.; Ding, B.; Chan, B.; Yu, M.; Kepert, C.J.; D'Alessandro, D.M. Through-space intervalence charge transfer as a mechanism for charge delocalization in metal–organic frameworks. *J. Am. Chem. Soc.* **2018**, *140*, 6622–6630.
57. Ramírez-Wierzbicki, I.; Cotic, A.; Cadranel, A. Photoinduced intervalence charge transfers: spectroscopic tools to study fundamental phenomena and applications. *ChemPhysChem* **2022**, *23*, e202200384.
58. Yang, C.; Guo, N.; Qu, S.; Ma, Q.; Liu, J.; Chen, S.; Ouyang, R. Design of anti-thermal quenching Pr³⁺-doped niobate phosphors based on a charge transfer and intervalence charge transfer band excitation-driven strategy. *Inorg. Chem. Front.* **2023**, *10*, 4808–4818.
59. Kong, L.; Jing, Z.; Mamoor, M.; Jiang, Y.; Zhai, Y.; Qu, G.; Wang, L.; Wang, B.; Xu, L. Enhancing the Reversibility and Kinetics of Heterovalent Ion-Substituted Mn-Based Prussian Blue Analogue Cathodes via Intervalence Charge Transfer. *Angew. Chem. Int. Ed.* **2025**, e202500254.
60. Chang, X.; Dong, X.; Liu, X.; Tong, Y.; Li, K.; Li, Z.; Lu, Y. Constructing a hexagonal/orthorhombic WO₃ phase junction for enhanced photochromism. *Opt. Mater.* **2023**, *142*, 114131.
61. Wang, Q.; Zhang, W.; Hu, X.; Xu, L.; Chen, G.; Li, X. Hollow spherical WO₃/TiO₂ heterojunction for enhancing photocatalytic performance in visible-light. *J. Water Process Eng.* **2021**, *40*, 101943.
62. Zhao, J.; Liu, L.; Zhang, Y.; Feng, Z.; Zhao, F.; Wang, W. Light-responsive color switching of self-doped TiO_{2-x}/WO₃·0.33H₂O hetero-nanoparticles for highly efficient rewritable paper. *Nano Res.* **2020**, *14*, 165–171.
63. Zhang, Y.; Cheng, C.; Zhou, Z.; Long, R.; Fang, W.H. Surface Hydroxylation during Water Splitting Promotes the Photoactivity of BiVO₄(010) Surface by Suppressing Polaron-Mediated Charge Recombination. *J. Phys. Chem. Lett.* **2023**, *14*, 9096–9102.
64. Deng, H.; Qin, C.; Pei, K.; Wu, G.; Wang, M.; Ni, H.; Ye, P. TiO₂/reduced hydroxylated graphene nanocomposite photocatalysts: Improved electron–hole separation and migration. *Mater. Chem. Phys.* **2021**, *270*, 124796.
65. Yang, Y.; Chen, Y.; Li, Y.; Wang, Z.; Zhao, H. Acid-, mechano- and photochromic molecular switches based on a spiropyran derivative for rewritable papers. *Mater. Chem. Front.* **2022**, *6*, 916–923.
66. Zhang, Y.; Wang, Q., Acceleration photochromic performance in tungsten oxide. *Opt. Mater.* **2024**, *157*, 116365.
67. Zhu, Y.; Li, B.; Li, C.; Tian, S., Transparent photochromic Fe-doped W₁₈O₄₉ films with ultrahigh solar energy modulation for smart windows. *J. Mater. Chem. C* **2025**, *13*, 6115–6122.
68. Oderinde, O.; Ejeromedoghene, O.; Fu, G., Synthesis and properties of low-cost, photochromic transparent hydrogel based on ethaline-assisted binary tungsten oxide-molybdenum oxide nanocomposite for optical memory applications. *Polym. Adv. Technol.* **2022**, *33*, 687–699.
69. Liu, T.; Li, J. L.; Xie, Z.; Huang, C.; Wang, J.; Zhang, C.; Sha, C.; Wang, L., Naphthalene-embedded spiropyran derivative-A type of conjugated expanded material with solid-state photochromic properties and tunable color switching range. *J. Mol. Struct.* **2024**, *1318*, 139404.